Article

Bacterial Hachiman complex executes DNA cleavage for antiphage defense

Yongqing Cui[1,2], Zhikang Dai[1,2], Yufei Ouyang[1,2], Chunyang Fu[1], Yanjing Wang[1], Xueting Chen[1], Kaiyue Yang[1], Shuyue Zheng[1], Wenwen Wang[1], Pan Tao [1], Zeyuan Guan [1] ✉ & Tingting Zou [1] ✉

Bacteria have developed a variety of immune systems to combat phage infections. The Hachiman system is a novel prokaryotic antiphage defense system comprising HamA and HamB proteins, which contains the DUF1837 and helicase domains, respectively. However, the defense mechanism remains only partially understood. Here, we present the cryo-electron microscopy (cryo-EM) structure of the Hachiman defense system featuring a fusion of Cap4 nuclease domain within HamA. Further structure analysis indicates that the DUF1837 domain on HamA resembles the PD-(D/E)XK nuclease but lacks active sites. Bioinformatics analysis reveals that catalytically inactive DUF1837 domains often recruit other functional domains to fulfill anti-phage defense. HamA interacts with HamB to form a heterodimer HamAB to mediate ATP hydrolysis and execute DNA cleavage, thus implementing antiphage defense. Our findings elucidate the structural basis of the Hachiman defense complex, highlighting the critical roles of the helicase and nuclease in prokaryotic immunity.

Bacteriophages, as viruses specifically infecting bacteria, constitute the most abundant organisms on Earth[1,2]. To proliferate in phage-rich environments, bacteria have evolved multiple defense mechanisms to counteract phage infection[3–5]. Phage defense systems in bacterial genomes are frequently clustered together and termed as "defense islands"[6]. In recent years, more than one hundred novel bacterial antiphage systems have been identified, such as Thoeris, cyclic oligonucleotide-based anti-phage signaling system (CBASS), retron, Gabija, RADAR, and pAgo[7–16]. These systems employ various strategies to inhibit the phage reproduction cycle, such as nucleic acid degradation, nucleotide modification, and membrane disruption[17–27]. Bacterial defense systems mainly including CBASS system, Avs system, Type III CRISPR system, and Lamassu system, all of which commonly utilize nucleases to combat invasive genetic elements, such as phages and plasmids, during the immune response process[9,12,28,29]. These nucleases tend to be part of large protein complexes with a variety of enzymatic activities[9,26–36]. Helicases and nucleases always work together to establish a cooperative defense against phage attacks[31,36–44].

Nhi, a nuclease-helicase protein, confers immunity against diverse *staphylococcal* phages and prevents phage DNA accumulation in cells[45]. The helicase/nuclease Hna provides defense against phages in *Sinorhizobium meliloti*[46]. The SF2 helicase/nuclease Cas3 can interfere virus in type I CRISPR-Cas systems[47,48]. However, the molecular basis of these defense systems containing nuclease and helicase domains remains to be fully explored.

The Hachiman system is a bacterial defense system, and it is distributed in ~4% of bacterial genomes encompassing nearly 2000 species[7]. This defense system comprises two genes: *hamA*, encoding a protein with a domain of unknown function (DUF1837), and *hamB*, encoding a protein with a predicted helicase domain. Based on bioinformatics analysis, Payne et al. classified the Hachiman systems that contain only HamA and HamB as type I, while 3.8% of Hachiman systems that include HamA, HamB, and HamC (DUF3223) were referred to as type II[49]. The Hachiman system has been reported to provide broad anti-phage defense functions[7,38,49,50]. For example, the Hachiman operon from *Bacillus cereus* B4087 is expressed in *Bacillus subtilis*,

[1]National Key Laboratory of Agricultural Microbiology, Hubei Hongshan Laboratory, Huazhong Agricultural University, Wuhan, China. [2]These authors contributed equally: Yongqing Cui, Zhikang Dai, Yufei Ouyang. ✉e-mail: guanzeyuan@mail.hzau.edu.cn; zoutingting@mail.hzau.edu.cn

conferring defense against three major families of *Bacillus* phages[7]. However, the related molecular mechanisms of Hachiman systems remain incompletely understood.

In this study, we constructed a phylogenetic tree based on 1781 representative HamA sequences identified by Doron et al.[7], classifying the type I Hachiman defense system into four distinct subtypes (type I-A to I-D). The type I-A Hachiman defense system contains only the DUF1837 domain in HamA, while the other three subtypes include an additional N-terminal domain. We determined the cryo-EM structure of the type I-B Hachiman defense system, which features a fusion of the N-terminal Cap4 nuclease domain within HamA. Structural analyzes reveal that the conserved DUF1837 domain in HamA resembles the PD-(D/E)XK nuclease, enabling the degradation of diverse DNA substrates. HamA recruits auxiliary functional domains, such as Cap4 endonuclease, for antiphage defense when its DUF1837 domain loses catalytic activity. HamB is a typical SF2 helicase with two RecA-like domains, exhibiting ATP hydrolysis activity in the presence of DNA, and this activity is significantly enhanced upon binding to HamA. HamA and HamB form a binary complex to exert antiphage activity collaboratively. Additionally, the HamAB complex in the type I-A Hachiman system also exhibits nuclease activity and contributes to phage defense functions.

Results

Hachiman system provides defense against phages

To investigate the anti-phage mechanisms of the Hachiman system, we initially analyzed this system located in the region of prophage CP4-57 in *Escherichia. coli* K12 strain, which comprises the HamA (AbpA) and HamB (AbpB) proteins[50]. HamA and HamB exhibit broad conservation across bacterial species. HamA comprises a predicted Cap4 endonuclease domain and a functionally unknown domain DUF1837, and HamB contains a DEAD-box helicase domain (Fig. 1a). The coding sequences of HamA and HamB overlap by four base pairs. We introduced the entire HamAB operon (along with its native promoter) into the pACYC184 plasmid and evaluated the HamAB-mediated defense against a panel of 50 phages using the *E. coli* strain (MG1655 Δ*hamAB*). Our results show that the Hachiman system in *E. coli* affords 10- to 10,000-fold protection against a broad spectrum of phages from various genes. HamAB shows a strong defense phenotype against Hanrirervirus and Warwickvirus phages with a >1000-fold efficiency of plating (EOP) reduction and against T1 and Dhilonvirus phages with a >100-fold EOP reduction, whereas a less strong defense phenotype against T7 and M13 phage (Fig. 1b and Supplementary Fig. 1).

To determine whether the Hachiman system functions through an abortive infection mechanism, we challenged the bacteria with phages at varying multiplicities of infection (MOIs). The Hachiman system demonstrated protection, particularly against phages T1 or TP041 at low MOIs, whereas at a high MOI, premature culture collapse occurred with the vast majority of cells infected by the initial TP041 phage attack (Fig. 1c, d), indicating that the Hachiman system operates through an abortive infection strategy, causing the death of infected cells before the maturation of phage progeny[51].

Cryo-EM structure of the Hachiman complex

To elucidate the defense mechanism underlying the Hachiman system, we determined the structure of the HamA and HamB complex using single-particle cryo-electron microscopy (cryo-EM). HamA generates a 538-amino acid (aa) protein, while HamB produces a 729-aa protein (Fig. 1e). The size-exclusion chromatography analysis showed that HamA and HamB were successfully assembled into a complex HamAB through the recombinant expression and purification (Supplementary Fig. 2a). Subsequently, we resolved the cryo-EM structure of the HamAB complex at a resolution of 3.1 Å (Supplementary Fig. 2b–e).

The cryo-EM structure of the HamAB complex reveals that HamA and HamB form a stable heterodimer in a 1:1 stoichiometry, with an interface area of ~2560 Å^2 (Fig. 1f, g). HamA comprises an N-terminal predicted nuclease domain (residues 1–252) and a C-terminal DUF1837 domain (residues 253–538, Fig. 1e). The N-terminal domain contains a central four-stranded mixed β-sheet edged by α-helices on each side, forming a scaffold for the active site assembly (Fig. 2a and Supplementary Fig. 3a). The structure and topology of N-terminal domain is a restriction endonuclease-like fold, with catalytic residues (aspartic acid, glutamic acid, and lysine) situated in a characteristic central β strand. Structural comparisons of the N-terminal domain and the restriction endonuclease HindIII-DNA complex show structural similarities and shared catalytic residues, suggesting that HamA belongs to the PD-(D/E)XK nuclease-like superfamily (Supplementary Fig. 3b)[52,53]. DALI analysis of the HamA N-terminal domain structure reveals its high similarity to the Cap4 and SeAvs3 nucleases, with Z-scores (the amount of structural similarity) of 11.9 and 10.7, respectively. These two nucleases separately serve as phage-activated DNA endonucleases in the CBASS and AVAST defense systems[9,28]. Sequence alignment of HamA-Cap4 and Cap4 enzymes from CBASS systems confirms the presence of all putative active-site residues (D45, Q58 and K60) essential for metal coordination (Fig. 2b and Supplementary Fig. 3c). In agreement with these observations, alanine substitutions at the conserved active sites within the HamA Cap4 nuclease motif resulted in the complete loss of Hachiman defense activity in *E. coli*[37] (Fig. 2c, d and Supplementary Fig. 3d). These data suggest that HamA might function as a PD-(D/E)XK nuclease enzyme.

The HamB protein encompasses three distinct domains, namely, N-terminal domain, helicase core, and C-terminal helical domain (Fig. 2e). The N-terminal domain of HamB exhibits similarity to the TPR (tetratricopeptide repeat) motif (Supplementary Fig. 4a, b), and this motif is characterized by pairwise alpha-helices linked by a loop, facilitating protein-protein interactions[54]. HamB, belonging to the super-family 2 (SF2) helicase family[55], contains RecA-fold domains 1 and 2 which collectively include 7 conserved helicase sequence motifs necessary for ATP hydrolysis and nucleic acid binding (Fig. 1e and Supplementary Fig. 5). The structure of the RecA domain of human RNA helicases RIG-I and MDA5 exhibit similarity to that of the RecA domain of HamB, with a root mean square deviation (RMSD) of 4.01 and 3.73 (over 168 Cα atoms), respectively (Supplementary Fig. 4c–e)[56,57]. Point mutations in the conserved residues that constitute the ATP binding site (G127A/K128A/S129A) in the helicase motif I completely abolished defense activity of HamAB (Fig. 2c, d, f). Taken together, these results suggest that the ATP binding is essential for the antiphage defense of the Hachiman system[37].

The structure of HamAB complex reveals that HamA and HamB adopt a heterodimer conformation via extensive hydrogen bonding and salt-bridge interactions across three distinct interfaces (interfaces 1, 2, and 3) (Fig. 2g). Interface 1 includes the Cap4 nuclease domain of HamA (residues 31-34) and the TPR1 repeat (residues 31-33) of HamB. Interface 2 comprises the Cap4 domain of HamA (residues 180-251) and the RecA1 domain of HamB (residues 256-271). Finally, Interface 3 consists of the DUF1837 domain of HamA (helices α8-10, strands β5/6/9) and the TPR domain (helices 2/4/6) of HamB (Fig. 2h).

To evaluate the importance of HamA-HamB interfaces, we examined HamA-HamB interactions and phage defense function through HamAB truncations and point mutations. Consistent with our observations of the HamAB complex structure, pull-down assays show that the truncation of the DUF1837 domain in HamA completely deprives HamA of its ability to bind to HamB in vitro. Likewise, the deletion of the TPR repeats from HamB hinders the in vitro formation of the HamAB complex (Supplementary Fig. 6a). Specifically, the HamA residues R428, L432, D437, E369, E374, Y367, D433, R346, D305, D316, and R328 show hydrogen bond interactions with HamB S18/N21, N27, Y36, H56, T57/T58, N62, K66, D83, R86, Y91 and R92, respectively (Fig. 2h). Consistent with the observed interaction mode of HamAB, alanine substitutions at residues N62/K66 and Y91/R92
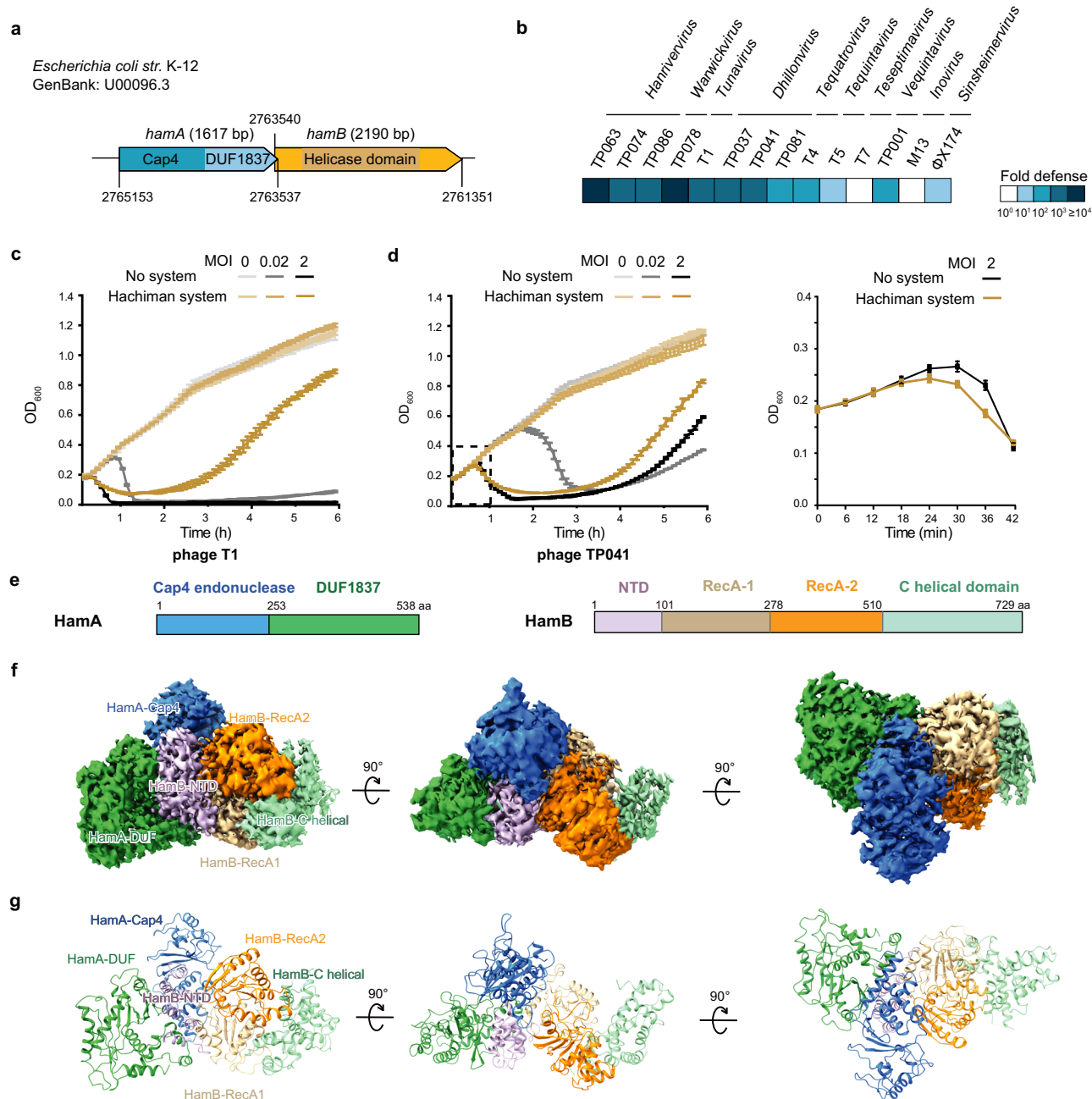
Fig. 1 | Hachiman system provides defense against diverse phages. a Schematic of the Hachiman system gene cassette from *Escherichia coli* strain K-12. **b** Anti-phage defense phenotype of *E. coli* strain MG1655 (Δ*hamAB*) expressing Hachiman system with a native promoter. Fold defense was measured through serial dilution spot test. Each assay was performed with two replicates (detailed data in Supplementary Fig. 1). Growth curves for *E. coli* MG1655 strain expressing the Hachiman system or an empty vector, infected with phages T1(**c**) or phage TP041 (**d**) at an MOI of 0, 0.02, or 2. Data are mean ± SD of three technical replicates and are representative of two independent experiments. **e** Domain organization of HamA and HamB proteins of Hachiman system from the *Escherichia coli* str. K-12 genome. **f** Cryo-EM density map of the HamAB complex. **g** Cartoon of structural model of the HamAB complex. Blue, HamA-Cap4 domain; Green, HamA-DUF1837; Purple, HamB-NTD; Brown, RecA-1 domain; Yellow, RecA-2; Cyan, HamB-C helical.

within the TPR repeats hinders the formation of the HamAB complex and diminishs the protection against phage infection (Fig. 2i and Supplementary Fig. 6b). These findings indicate that the N-terminal TPR domain of HamB is responsible for HamA binding and phage defense, which is in line with a recent report on Hachiman system[38]. Mutations in the DUF1837 domain of HamA (D305A, R346A, R428A, and D433A/D437A) result in loss or decrease of phage resistance (Fig. 2i). Thus, these results highlight the essential role of the complex assembly of HamA and HamB in anti-phage defense via the Hachiman system.

ATPase activity is critical for the Hachiman function

Helicases are characterized by a set of essential conserved motifs integral to their activity. These enzymes typically comprise two RecA-like domains responsible for ATP binding and hydrolysis[55]. Considering the pivotal role of ATP binding sites in the antiviral function of the Hachiman system, we performed a malachite green assay in vitro to investigate HamB's ATPase activity. Since nucleic acid often enhances the ATPase activities of helicases, we examined ATP hydrolysis with various DNA and RNA substrates. The results indicate that HamB catalyzes the release of inorganic phosphate from ATP, with 52-bp dsDNA
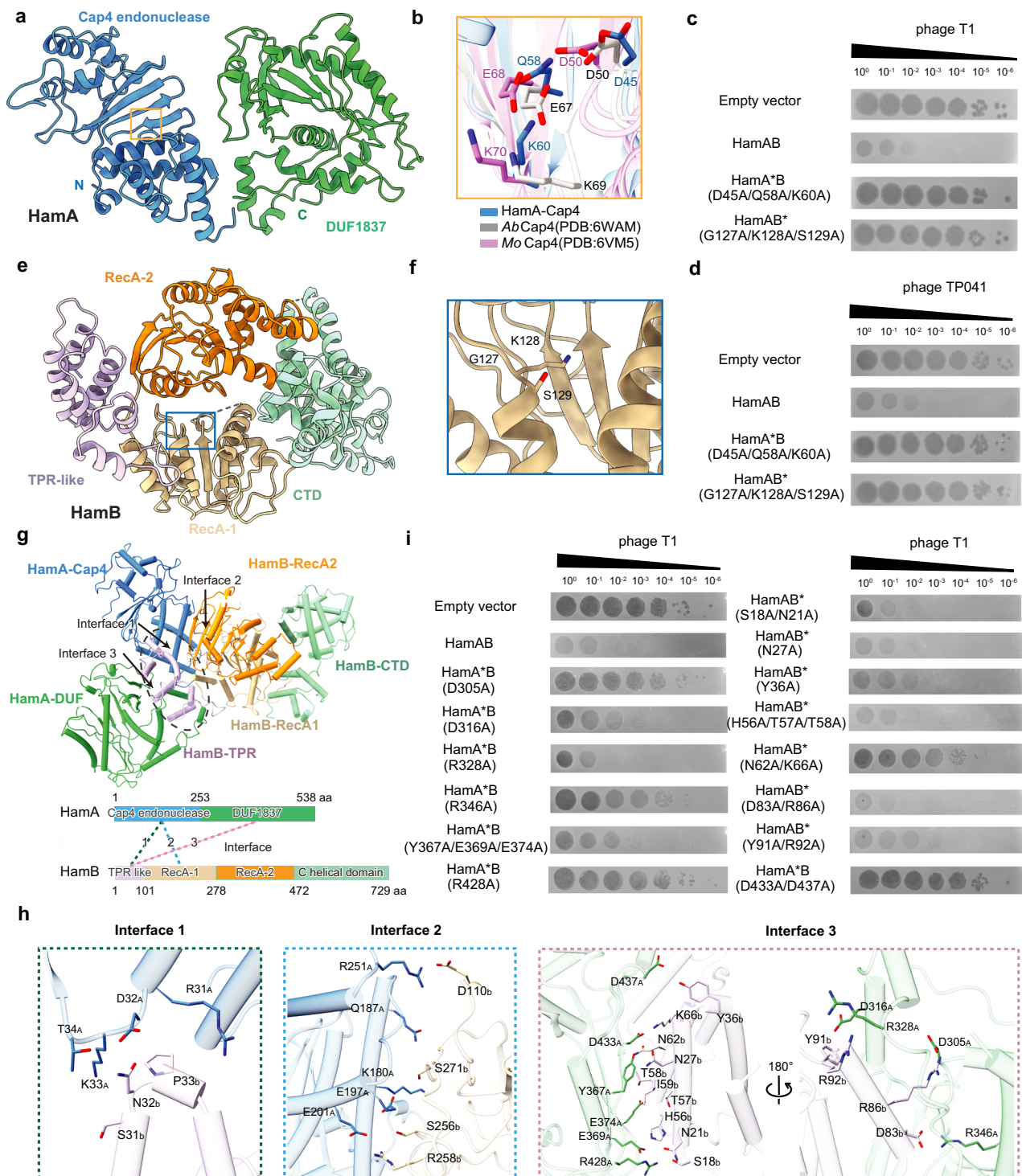
Fig. 2 | Cryo-EM structure of the HamAB complex. a Cartoon schematic and cryo-EM structure of HamA in HamAB complex. HamA contains an N-terminal Cap4 endonuclease domain (blue) and a C-terminal DUF1837 domain (green). **b** Enlarged view of the nuclease active sites of Cap4 endonuclease domain. Phage spot test of phage T1 (**c**) and phage TP041 (**d**) infection on *E. coli* strain MG1655 containing empty vector, Hachiman system, or mutant Hachiman systems, with three biological replicates. Source data are provided as a Source Data file. **e** Cartoon schematic and cryo-EM structure of HamB in HamAB complex. **f** Enlarged view of key residues mediating HamB ATP binding. **g** Interactions between HamA and HamB. The insets indicate the three key interfaces (Interface 1, 2, and 3). **h** Enlarged views of Interface 1, Interface 2, and Interface 3, exhibiting key residues on the interfaces. **i** Phage spot test of T1 phage infection on *E. coli* MG1655 expressing wild-type Hachiman system (HamAB) or expressing mutant HamA/HamB, with two biological replicates. Source data are provided as a Source Data file.

fragment as substrate. Conversely, substrates such as 52-nt ssDNA, pUC19 plasmid dsDNA, phage ΦX174 ssDNA, 1200 bp dsDNA, and 21-nt ssRNA fail to significantly enhance HamB's ATPase activity. Mutation of the ATP binding sites of HamB led to a complete loss of ATPase activity (Fig. 3a). To explore the effects of HamA on HamB ATPase activity, we

quantified the release of inorganic phosphate from ATP hydrolysis based on the assays of HamA, HamB, and HamAB complex, respectively. Our analysis demonstrates that the ATPase activity of HamAB complex is significantly enhanced in the presence of 52-bp dsDNA, showing an almost tenfold increase relative to that of HamB alone
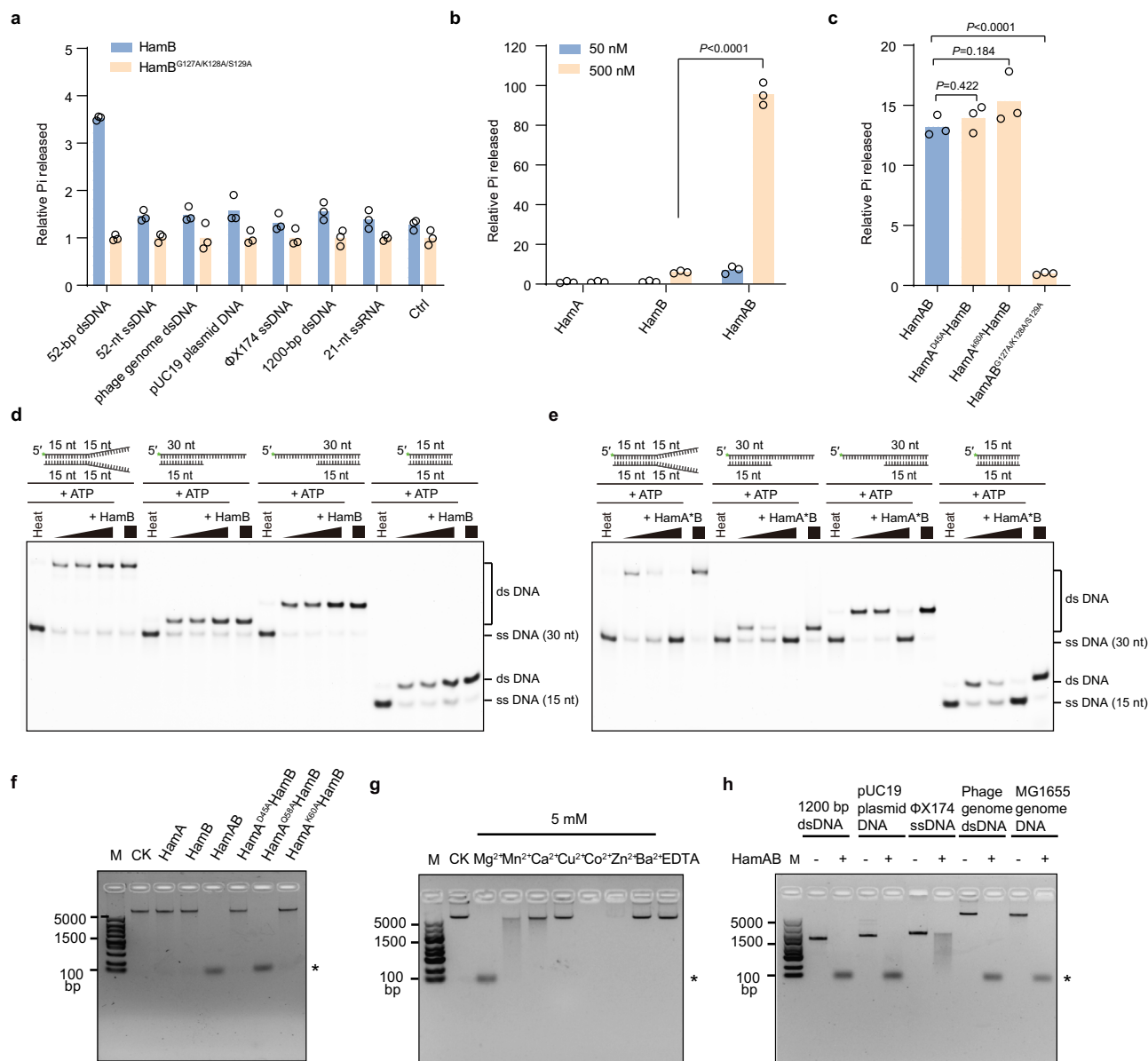
Fig. 3 | ATPase and nuclease activity of HamAB complex. a ATPase activity assay of HamB in the presence of various DNA and RNA substrates, including 52-bp dsDNA, 52-nt ssDNA, phage TP041 genome dsDNA, pUC19 plasmid DNA, phage ΦX174 genome ssDNA, PCR-amplified pUC19 1200-bp DNA, and 21-nt ssRNA (sequences listed in Supplementary Table 2). **b** ATPase activity of HamA, HamB, and HamAB complex proteins at 50 nM and 500 nM concentrations in the presence of 52-bp dsDNA. All reactions were performed at 30 °C for 30 min. Data are shown as the mean ± SD ($n = 3$). Two-sided Student's t-test was used for statistical analysis. P values are indicated above the plots. $P < 0.05$ was considered statistically significant. **c** ATPase activity of HamAB and its mutants in the presence of 52-bp dsDNA. Data are shown as the mean ± SD ($n = 3$). Two-sided Student's t Test was used for statistical analysis. P values are indicated above the plots. $P < 0.05$ was considered statistically significant. DNA unwinding assays of HamB (**d**) and HamA*B (**e**) on substrates with a 15 bp duplex and forked 15 nt, 15 nt 3′ overhang, 15 nt 5′ overhang, or no overhang. DNA substrates are labeled with 5′ FAM. Substrates

heated to 95 °C for 10 min were used as a positive control. Native gels are representative of three independent replicates. **f** Nuclease activity of HamA, HamB, HamAB complex, and HamAB mutant proteins. All reactions were performed at 37 °C for 30 min. Phage genome DNA was used as the substrate. These experiments were performed three times with equivalent results, and the representative results were shown. **g** Nuclease activity of HamAB in the presence of different metal ions, including $MgCl_2$, $MnCl_2$, $CaCl_2$, $CuCl_2$, $CoCl_2$, $ZnCl_2$, or $BaCl_2$. All reactions were performed at 37 °C for 30 min. Phage genome DNA was used as the substrate. These experiments were performed twice with equivalent results, and the representative results were shown. **h** DNA cleavage activity by HamAB in the presence of different substrate DNAs, including PCR-amplified pUC19-1200 bp DNA, pUC19 plasmid DNA, ΦX174 genome ssDNA, TP041 phage genome dsDNA, and MG1655 bacteria genome dsDNA. Black stars indicate the cleavage products. These experiments were performed three times with equivalent results, and the representative results were shown.

(Fig. 3b). In addition, the mutations of the conserved catalytic sites in HamA do not affect HamAB ATPase activity, whereas the mutation of ATP binding sites in HamB results in a complete loss of hydrolysis activity of HamAB (Fig. 3c). This indicates that ATP hydrolysis by HamB is essential for Hachiman activity, which is in accordance with our phage infection assay (Fig. 2c, d).

The HamB structure reveals an SF2 helicase core containing two RecA-like helicase domains. To determine whether HamB possesses helicase activity, we incubated HamB with various DNA duplexes in the presence of ATP and Mg^{2+}. The results show that HamB does not unwind overhang substrates or blunt dsDNA, with helicase activity undetectable (Fig. 3d). Since HamAB complex exhibits a higher ATP

hydrolysis activity than HamB, we further tested DNA unwinding by HamA*B (D45A/Q58A/K60A, HamA nuclease inactive mutant) complex. In contrast, HamA*B can unwind various substrates incubated with overhang or blunt dsDNA containing a 15-bp duplex (Fig. 3e). These results demonstrate that HamA coordinates with HamB to unwind dsDNA.

Nuclease activity of the HamAB complex

Further, we evaluated the ability of HamA and HamAB proteins to cleave DNA substrates in vitro. After incubating with a dsDNA substrate, HamA exhibits no nuclease activity. In contrast, the HamAB complex effectively catalyzes the complete degradation of dsDNA into fragments smaller than 100 bp. Moreover, the mutation of conserved active sites of the HamA (D45A or K60A) eliminates nuclease activity of HamAB, indicating that the N-terminal Cap4 nuclease domain of the HamA is of cleavage capacity, but it is auto-inhibited in the full-length protein (Fig. 3f). Additionally, the nuclease function of the HamAB complex is dependent on Mg^{2+}, Co^{2+}, or Zn^{2+}, but independent of Ca^{2+}, Cu^{2+}, and Ba^{2+} ions (Fig. 3g). The HamAB complex degrades a wide range of DNA, including linear dsDNA, plasmid DNA, ΦX174 ssDNA, phage genome dsDNA, and bacterial genomic DNA, as indicated by clear degradation bands (Fig. 3h). Overall, these findings suggest that the Hachiman complex adopts a Cap4 enzyme-like reaction mechanism to degrade nucleic acids.

DUF1837 is a PD-(D/E)XK nuclease domain in the Hachiman defense system

DUF1837, the C-terminal of the HamA protein, remains functionally uncharacterized. Structural analysis of HamA reveals that the DUF1837 domain comprises a central five-stranded β sheet decorated on either side by alpha helices, which resembles the core motif of the proteins in the PD-(D/E)XK phosphodiesterase superfamily (Fig. 4a). The top hit of DALI search for DUF1837 is type II restriction endonuclease PaqCI, with a Z score of 5.6. The active site core is the PD-(D/E)XK motif, essential for phosphodiester bond cleavage in nucleic acids. Our analysis reveals the absence of these active sites in the DUF1837 domain of HamA. In contrast, in a different Hachiman defense system from *E. coli* DEC14B, the structure (predicted by AlphaFold2) of DUF1837 domain of HamA closely resembles that of PaqCI nuclease, but DUF1837 domain includes all the active sites of PD-(D/E)XK nuclease family (Fig. 4a and Supplementary Fig. 7a)[58]. Sequence alignment classifies DUF1837 domain of HamA into two categories: one with conserved active sites and the other without catalytic active sites (Supplementary Fig. 7a).

To better understand the HamA diversity in Hachiman defense systems, we generated a phylogenetic tree based on 1781 representative sequences identified by ref. 7. The phylogenetic tree shows that the HamA proteins are clustered into four distinct clades. Among them, type I-A contains only the DUF1837 domain, with conserved active sites, constituting the majority clade (1539 of 1781, accounting for 86.4%), whereas type I-B, type I-C, and type I-D are characterized by an additional N-terminal domain apart from the DUF1837 domain (Fig. 4b, c). This additional domain contains predicted Cap4 nucleases, peptidases, or other unidentified domains (hereafter referred to as "X"), with its average length ranging from 87 to 577 amino acids (Fig. 4b, d). We observed that the PD-(D/E)XK sites are absent in the DUF1837 domains of type I-B, type I-C, and type I-D, based on which we speculated that these DUF1837 domains might be catalytically inactive, functioning as scaffolds.

To assess the protective capacity of type I-A Hachiman systems against phage infection, we investigated the defense activity of the HamAB complex (from *E. coli* strain DEC14B) comprised of HamA containing only a DUF1837 domain and HamB containing a helicase domain (Fig. 4e). We cloned the HamAB operon along with its native promoter into plasmid pACYC184, and subsequently introduced plasmid pACYC184 into *E. coli* MG1655 ΔhamAB, followed by challenge

with various *E. coli* phages. The results show that the type I-A Hachiman system provides a protective effect against seven distinct dsDNA bacteriophages, including model phages T4 and T7 (Supplementary Fig. 7b, c). In addition, the mutation of the active sites E150A and K152A in HamA results in a loss of functionality, suggesting that the nuclease activity of the DUF1837 domain is crucial for this defense. A point mutation (G272A/K273A/T274A) of the helicase domain in HamB impedes ATP binding, thereby eliminating the protective effect of the Hachiman system (Fig. 4f).

Given that the DUF1837 domain exhibits structural homology with type II restriction endonucleases, we hypothesize that HamA DUF1837 is a PD-(D/E)XK nuclease family member. To evaluate the nuclease activity of the type I-A Hachiman system in vitro, HamA and HamB were recombinantly expressed and purified from *E. coli*. The co-expression and purification experiments confirm the formation of HamAB complex (Supplementary Fig. 7d). Incubation of HamA and HamAB with linear double-stranded DNA showed progressive substrate degradation only in the presence of HamAB, which is in line with the observation of the type I-B Hachiman system from *E. coli* K-12. The nuclease activity of HamAB is dependent on the catalytic residues of HamA-DUF1837, and it is abolished by the E150A/K152A nuclease mutation in HamA, which is consistent with results of phage spot test (Fig. 4f, g). Further, we investigated the substrate specificity of type I-A Hachiman system and found that HamAB effectively degraded various DNA substrates, including 1200-bp double-stranded DNA (dsDNA), supercoiled pUC19 plasmid DNA, ΦX174 ssDNA, phage genome dsDNA, and MG1655 genome DNA, yielding the fragments ~100 nucleotides in length. This result suggests that HamAB has a non-specific nuclease activity (Fig. 4h). Taken together, these results collectively support the hypothesis that the DUF1837 domain acting as a PD-(D/E)XK-like nuclease is essential for phage defense in the type I-A Hachiman system.

Discussion

The Hachiman system provides protection against phage infection in host cells through an abortive infection mechanism. Here, we investigated bacterial type I-A and type I-B Hachiman defense systems, revealing that both subtypes have broad-spectrum anti-phage functions, which are mediated by two proteins, namely, HamA with DNA endonuclease activity and HamB as an SF2-type helicase. All HamA proteins possess a DUF1837 domain. Structural analysis reveals that this domain is part of the PD-(D/E)XK nuclease family. Specifically, in the type I-A Hachiman system, the DUF1837 domain includes all conserved catalytic sites essential for its function. In contrast, in the type I-B, I-C, and I-D systems, the DUF1837 domain displays a structure similar to the PD-(D/E)XK nuclease, but it lacks catalytic sites and is integrated with other domains to act as effector proteins, which is crucial for phage resistance. Our data suggest that HamA alone exhibits no nuclease activity in the presence of diverse nucleic acid substrates. Likewise, HamB alone does not exhibit helicase activity, either. However, when HamA binds with HamB to form the HamAB complex, this complex undergoes DNA unwinding through ATP hydrolysis, exerting DNA degradation activities. A recent study by Tuck et al. showed that HamA and HamB, classified as part of the type I-A Hachiman system, can form a heterodimeric nuclease-helicase complex. Upon detecting DNA damage, the activated Hachiman system degrades both phage and host DNA[38]. These results collectively indicate that the formation of the HamAB complex is crucial for resistance against phage infection (Fig. 4i).

Tuck et al. indicated that HamB from the type I-A system can detect DNA damage, recognize and bind to 3' ssDNA ends to trigger ATPase activity, further activating HamA to exert nuclease activity[38]. However, our data suggest that the ATPase activity of HamB in the type I-B Hachiman system is significantly activated by dsDNA. Phylogenetic analysis shows that type I-A and type I-B HamB occupy
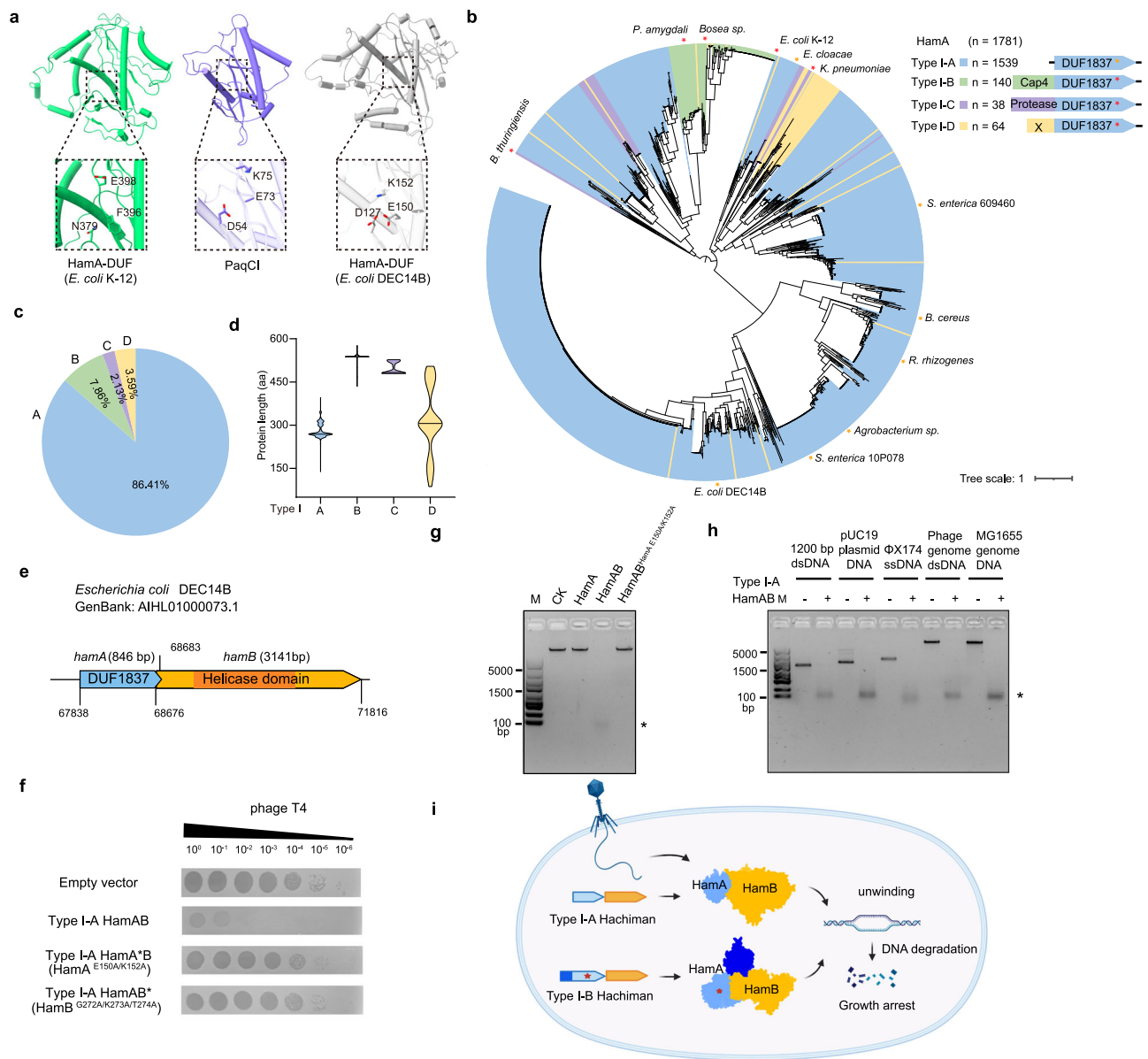
Fig. 4 | DUF1837 belongs to the PD-(D/E)XK nuclease family. a Structural alignment of the DUF1837 domain from the HamA, PaqCI (PDB: 8EPX), and HamA-DUF (AlphaFold 2, *E. coli* DEC14B). **b** Phylogenetic tree of HamA proteins with putative DUF1837 domains, based on 1781 sequences. The yellow asterisk indicates the presence of the (D/E)xK motif in HamA, and the red asterisk denotes its absence. **c** Percentage of type I-A (blue), type I-B (green), type I-C (purple), and type I-D (yellow) Hachiman systems. **d** Violin plots of the polypeptide length distribution of different types of Hachiman systems. Solid black lines indicate the median length. **e** Domain organization of HamA and HamB genes in the type I-A Hachiman system from the *Escherichia coli* strain DEC14B. **f** Phage spot test of phage T4 infection on the *E. coli* strain MG1655 containing empty vector, the type I-A Hachiman system, or mutant Hachiman systems. Each assay was repeated three times. Source data are provided as a Source Data file. **g** Nuclease activity of the type I-A HamA, HamAB complex, and mutant proteins. All reactions were conducted at 37 °C for 30 min. Phage genome DNA was used as the substrate. These experiments were performed twice with equivalent results, and the representative results were shown. **h** DNA cleavage activity by the type I-A HamAB in the presence of different substrate DNAs, including PCR-amplified pUC19-1200 bp DNA, pUC19 plasmid DNA, ΦX174 genome ssDNA, TP041 phage genome dsDNA, and MG1655 bacterial genome dsDNA. These experiments were performed twice with equivalent results, and the representative results were shown. Black stars indicate the cleavage products. **i** A proposed mechanism for Hachiman defense. Imaging was created in BioRender. Zou, T. (2025) https://BioRender.com/z35j180.

distinct branches, indicating significant sequence divergence (Supplementary Fig. 8a). Structural analysis reveals that while both subtypes share conserved DNA-binding amino acids, type I-B lacks the winged-helix (WH*) and oligonucleotide-binding (OB) fold domains present in type I-A (Supplementary Fig. 8b, c)[59,60]. The OB-fold domain, crucial for binding single-stranded nucleic acids, is absent in type I-B, suggesting differences in substrate specificity[61,62]. These structural and sequence variations likely explain why the ATPase activity of the two subtypes is triggered by different substrates.

Our findings indicate that the loss of nuclease activity in the effector DUF1837 domain prompts the Hachiman immune system to recruit an auxiliary effector to sustain antiphage defense. Furthermore, we hypothesize that the DUF1837 domain may function as a scaffold for assembling a multiprotein complex containing active homologs. This hypothesis is supported by our observation that the DUF1837 domain of HamA facilitates the assembly of the HamAB complex. Additionally, our data demonstrate that the ATP hydrolytic activity of the HamAB complex is significantly higher than that of HamB alone (Fig. 3b), aligning with recent results[38]. However, a discrepancy exists

between the two studies: in their research, the mutation of the nuclease active sites in HamA of the type I-A Hachiman system markedly influences HamAB ATP hydrolysis activity[38]. In contrast, the mutation of Cap4 nuclease active sites in HamA of the type I-B Hachiman system does not affect the ATP hydrolysis activity of HamAB (Fig. 3c). This suggests that the inactive DUF1837 domain acts as an intermediate to mitigate direct influence between the two catalytic domains, thereby significantly increasing the probability of DUF1837 fusing with other domains, such as peptidases, ultimately broadening the diversity of immune mechanisms in bacteria. Similarly, the prokaryotic Argonaute immune system employs various effector domains for antiviral defense due to the absence of nuclease activity in its PIWI domain[11,63]. Based on this, we speculate that bacteria adopt this strategy to enhance their defensive arsenal through long-term evolution against phages.

Methods

Bacterial strains, phages, and plasmids construction

The full-length of type I-B *hamAB* genes were amplified from the *Escherichia coli str.* K-12 (2761204–2765368 of GenBank Accession U00096.3). The full-length of type I-A HamAB genes from *Escherichia coli* DEC14B (67654–71936 of GenBank Accession AIHL01000073.1) were synthesized. For the construction of HamAB complex plasmids: (1) The *hamA* was subcloned into a pET15D vector (Novagen) between the NdeI and XhoI restriction sites, resulting in a fused protein with an N-terminal 6× His tag. The HamB gene was subcloned into the pBB75 vector (Novagen) without any tag between the NdeI and EcoRI restriction sites. (2) The Type I-*A hamA* gene was subcloned into the pBB75 vector (Novagen) without any tag, and the *hamB* was subcloned into a pET21b vector (Novagen) with a C-terminal 6×His-tag between the NdeI and EcoRI restriction sites. Plasmids encoding HamA and HamB were co-transfected in *E. coli* strain BL21(DE3). For the construction of individual HamA and HamB plasmids: The HamA was subcloned into a pET21b vector (Novagen) with a C-terminal 6×His-tag; The HamB was subcloned into a pET15D vector (Novagen) with an N-terminal 6×His-tag. HamA and HamB mutants were amplified by Fusion PCR. Plasmids encoding HamA or HamB were transfected in *E. coli* strain BL21(DE3). The Hachiman genetic unit with its native promoter was amplified from its native host and subcloned into pACYC184 vectors for the in vivo experiments (plasmids used in the study see Supplementary Data 1 and primer used for cloning see Supplementary Data 2). Except for the model bacteriophage, the other collections were isolated from sewage samples on *E. coli* MG1655 (phage information see Supplementary Data 3), as previously described[64]. All primers were chemically synthesized and purchased from Sangon Biotech.

Protein expression and purification

For the preparation of HamAB complex, the HamA and HamB, or the boundary and mutants, were co-expressed in *E. coli* strain BL21(DE3) using Lysogeny broth (LB) medium. The cells were induced by the addition of isopropyl-β-D-thioacetamide (final concentration of 200 μM) when OD_{600} reached 1.1, and induction was performed at 16 °C for 16 h. For HamAB complex (from the *E. coli* K-12 and *E. coli* DEC14B), HamA protein (from the *E. coli* DEC14B), and HamB protein (from the *E. coli* K-12) purification, the harvested cells were resuspended in lysis buffer containing 25 mM Tris-HCl (pH 8.0) and 150 mM NaCl. The lysate was disrupted using a homogenizer (JNBIO), and the cell debris was removed via centrifugation at $20,000 \times g$ for 1 h at 4 °C. The target protein was purified over Ni^{2+} nitrilotriacetate affinity resin (Ni-NTA, Qiagen) and eluted with Elution buffer (25 mM Tris-HCl pH 8.0, 250 mM imidazole). The eluted protein was further purified using ion-exchange chromatography (Source 15Q 10/100, GE Healthcare). The purified protein was concentrated and subsequently purified by gel filtration chromatography (Superose 6 10/

300; GE Healthcare) in SEC buffer (25 mM Tris-HCl pH 8.0, 150 mM NaCl, 5 mM dithiothreitol). The purity of the proteins was examined by SDS-polyacrylamide gel electrophoresis and visualized by Coomassie blue staining. The mutant proteins were purified similarly to the wild-type proteins. For the HamA protein (from the *E. coli* K-12) purification, the collected cells were resuspended in lysis buffer (25 mM Tris-HCl, pH 8.0, 1.5 M NaCl) and subsequently disrupted by pressure homogenizer at 4 °C. The target protein was purified over Ni^{2+} affinity resin, Source 15Q10/100, and Superose 6 10/300 columns used in tandem. The Elution buffer and SEC buffer of purified HamA remains consistent with the above.

Cryo-EM grid preparation and data acquisition

For cryo-EM data acquisition of the HamAB complex (*E. coli* K-12), 3.5 μl sample was dropped onto glow-discharged holey carbon grids (Quantifoil Au R1.2/1.3, 300 mesh). After blotting for 4.5 s with 100 % humidity at 8 °C, the grids were plunge-frozen in liquid ethane cooled by liquid nitrogen in Vitrobot Mark IV (ThemoFisher Scientific). Subsequently, the cryo-grids were screened using 300 kV Titan Krios electron microscopes (Thermo Fisher Scientific) and equipped with a Gatan K3 Summit Detector positioned to post a GIF Quantum Energy Filter (slit width 20 eV). Images for the HamAB were recorded in the counting mode with a magnification of 81,000× and collected with a pixel size of 1.07 Å and a defocus range of −1.2 to −2.2 μm. Each micrograph stack, which contains 32 frames, was exposed for 3.5 s with a total electron dose of 50 e⁻ Å⁻². Preliminary data processing results show that the HamAB exhibit strong preferential orientation on cryo-EM grids. Therefore, 6881 and 4864 cryo-EM micrographs were collected at 0° and 30° specimen tilt, respectively[65]. EPU software was used for fully automated data collection.

Cryo-EM data processing

A diagram of the procedures for data processing is presented in Supplementary Fig. 2. The movies collected at tilt angles of 0 and 30 degrees are separately motion corrected by Motioncor2 with 7 by 7 patches and CTF estimated by cryoSPARC patch CTF estimation[66]. From the datasets at 0° and 30°, 5752 and 3062 micrographs, respectively, were manually selected and merged into a total of 8814 micrographs for subsequent processing. A total of 3,516,428 particles were automatically picked using cryoSPARC blob picker, and the particle picking was optimized by Topaz software[66,67]. The particles underwent multiple rounds of 3D classification. In brief, the particles were extracted into a box of 240 Å and then binned by 4, 2, and 1, respectively, facilitating the 3D classification. Following the 3D classification, the well-classified particles were merged, deduplicated, and re-extracted. From the classification results of the original-sized particle images, 440,333 particles (~26.4% of the total) were selected for 3D refinement, resulting in a cryo-EM density map with an overall resolution of 3.1 Å based on gold-standard Fourier shell correlation (FSC)[68]. The local resolution of the map was estimated to be 2.8 to 4 Å using Resmap (v1.1.4)[69].

Model building and refinement

The initial model of HamA and HamB predicted by AlphaFold2[70] was rigidly docked to fit into the cryo-EM density map of HamAB, resulting in the acquisition of the initial coordinates file for the HamAB complex structure. The initial model of the HamAB complex was manually adjusted using COOT[71], and invisible segments were removed, yielding an optimized model that included the 7-537 segment of HamA, the 2-449 segment of HamB, and the 510-728 segment of HamB. The complex models were refined against the map using PHENIX in real space with secondary structure and geometry restraints[72]. Model quality was evaluated using the MolProbity scores[73], the Ramachandran plots, and EMRinger (see Supplementary Table 1)[74]. Figures were generated using ChimeraX v.1.2.5 and PyMol v.2.5.1.

In vitro pull-down assay

A co-expression coupled Ni-NTA pull-down assay was performed to detect the interaction of HamA and HamB. In this system, no tag HamB and 6×His-tagged HamA (wild-type or the boundary and mutants) were co-expressed within *E. coli* strain BL21(DE3). Then, the cell debris of the lysed cells and supernatant were loaded on Ni-NTA beads. After washing unbound proteins, the His-tagged HamA and interacting HamB were co-eluted by using an elution buffer (25 mM Tris-HCl pH 8.0, 250 mM imidazole). Elution was analyzed by SDS-polyacrylamide gel electrophoresis and revealed key residues for the interaction between HamA and HamB.

DNA degradation assays

DNA nuclease assays were carried out on various DNA in 20 μl reaction buffer (25 mM Tris-HCl pH 8.0, 5 mM $MgCl_2$, and 1 mM DTT) with 80 nM protein. The reactions were performed at 37 °C for 30 min and stopped by the addition of 2 μl 6× loading buffer (60 mM EDTA, 20 mM Tris-HCl pH 7.5, 30% glycerol, 0.1% SDS). After the reactions, products were separated on a 1.0% TAE agarose gel and run at 150 V for 20 min. The Gels were visualized using a Gel Doc™ Molecular imager (BIO-RAD). Source data are provided as a Source data file.

ATPase assay

The ATPase reactions were carried out in 20 mM Tris-HCl pH 7.5, 10 mM $MgCl_2$, and 1 mM DTT. We added 500 nM or 50 nM protein in a 20 μL reaction volume containing 2 mM ATP, 50 nM or 100 ng DNA substrate at 30 °C for 30 min. The release of inorganic phosphate (Pi) was monitored by Malachite Green Phosphate Assay as previously described[75]. The reaction products were measured by adding 150 μL malachite green solution (86 μL of 28 mM ammonium heptamolybdate in 2.1 M H_2SO_4 and 64 μL of 0.76 mM malachite green in 0.35% polyvinyl alcohol). After 10 min, absorption at 595 nm was monitored.

Helicase assays

To prepare substrates of double-stranded DNA (dsDNA) with 15 bp duplexes and a forked 15 nt OH, 15 nt 3′ OH, 15 nt 5′ OH, and no overhang for helicase assays, 5′ FAM-labeled single-stranded DNA (ssDNA) and unlabeled complementary ssDNA (see Supplementary Table 2 for oligonucleotide information) were mixed in a 1:2 molar ratio, denatured at 95 °C for 5 min, and annealed at 25 °C. For helicase assays, 40 nM 5′ FAM-labeled dsDNA substrates were incubated with HamB or HamA^{K60A}B at indicated concentrations (200 nM, 40 nM, and 8 nM) and 2.5 mM ATP in helicase buffer (20 mM Tris-HCl pH 8.0, 1 mM DTT, and 5 mM $MgCl_2$) supplemented with 1 μM unlabeled ssDNA (corresponding to the 5′ FAM-labeled ssDNA) to prevent reannealing. 10 μL reaction mixtures were incubated at 30 °C for 15 min, and then the unwinding reactions were stopped by adding 25 mM EDTA to the mixtures. Reactions without ATP served as negative controls. The reaction mixtures without proteins were incubated at 95 °C for 10 min as positive controls for unwinding. Samples were resolved on a 12% Tris-glycine polyacrylamide gel at 150 V for 5 h at 4 °C. The fluorescent signal of FAM-labeled DNA was detected using a Typhoon FLA-5100 scanner (Fujifilm Life Science, Japan). FAM-labeled DNA were synthesized and purchased from GenScript.

Phylogenetic analysis of HamA

According to the Hachiman systems identified in a previous study[7], 1781 protein sequences of HamA used in this study were downloaded from the NCBI database (https://www.ncbi.nlm.nih.gov/sites/batchentrez). The multiple sequence alignment was conducted using MAFFT version 7.310 with an automatic model[76], followed by automated alignment trimming using trimAl version 1.4[77]. Subsequently, a phylogenetic tree based on the trimmed sequence alignment was constructed using IQ-TREE version 2.0.3 with parameters -m MFP

(ModelFind plus) -bb 1000 (1000 iterations of the ultrafast bootstrap)[78]. The tree was visualized using iTOL[79]. Additional domains beyond DUF1837 within HamA were analyzed using the tools HHpred[80] and NCBI's Conserved Domain Database (CCD) with default parameters[81].

Bacterial liquid growth assays

Bacterial growth curves were measured in liquid media. The *hamAB* gene from *Escherichia coli* strain K-12 was cloned into the pACYC184 vector. The recombinant vectors were transformed into *E. coli* MG1655 (Δ*hamAB*) strain. An empty vector was used as a control. A single bacterial colony was picked from a fresh LB agar plate and grown in LB broth supplemented with chloramphenicol (25 mg mL^{-1}) at 37 °C. Overnight cultures were diluted 1:100 into a liquid LB medium containing chloramphenicol (25 mg mL^{-1}) and grown at 37°C for 2 h to an OD_{600} of about 0.18–0.2. Subsequently, MG1655 (Δ*hamAB*) strain harboring the *hamAB* gene cassette or the empty vector was infected with phages T1 or TP041 at $t = 0$ at a multiplicity of infection (MOI) of 0, 0.02, or 2. Growth was monitored using a FLUOstar Omega for 6 h at 30 °C with OD_{600} readings every 6 min. Graphs were produced using GraphPad Prism 8 software.

Phage spot test

The phage was propagated by picking a single phage plaque into a liquid culture of *E. coli* MG1655 grown at 37 °C in LB medium supplemented with 0.1 mM $MnCl_2$ and 5 mM $MgCl_2$. The culture was centrifuged for 10 min at 2000 × *g*, and the supernatant was filtered using a 0.45 μM filter to remove bacterial debris. The phage was then amplified and purified. The reconstructed pACYC184 plasmid was transformed into *E. coli* MG1655 (Δ*hamAB*) strain, *E. coli* JM109 strain (as the sensitive host bacteria for M13 phage), and DMB127 strain (as the sensitive host bacteria for ΦX174 phage). Different bacteria strains were incubated with chloramphenicol (25 mg mL^{-1}) at 37 °C. After overnight incubation, 500 μl of the bacterial culture was mixed with 4.5 ml molten top agar (containing 10 g L^{-1} tryptone, 5 g L^{-1} yeast extract, 10 g L^{-1} NaCl, and 5 g L^{-1} agar), and the entire samples were poured onto LB plates containing antibiotic. Phage solution was diluted in LB at seven 10-fold serial dilutions, namely, 10^0–10^{-6}. After the top agar had solidified, 2 μl drops of the diluted phage culture were spotted on the bacterial layer. Plates were incubated at 30 °C overnight and then imaged. Source data are provided as a Source data file.

Statistics and reproducibility

Statistical analyzes were performed using GraphPad Prism 8 (GraphPad Software Inc., USA). Sample sizes were chosen according to similar experiments published in previous literatures[38,39]. Multi-group comparisons were determined by Two-sided Student's *t*-test. All data are presented as the mean ± SD of three replicates, and $p < 0.05$ was considered statistically significant. All *P* values are indicated above the plots.

Reporting summary

Further information on research design is available in the Nature Portfolio Reporting Summary linked to this article.

Data availability

The atomic coordinates and EM density for the reported structures of the HamAB complex (PDB: 8ZUE; EMDB: EMD-60482) have been deposited in the Protein Data Bank (www.rcsb.org) and the Electron Microscopy Data Bank (www.ebi.ac.uk/pdbe/emdb/). All data needed to evaluate the conclusions in the paper are present in the paper and/or the Supplementary Materials. Additional data related to this paper may be requested from the authors. Source data are provided with this paper.

References

1. Salmond, G. P. C. & Fineran, P. C. A century of the phage: past, present and future. *Nat. Rev. Microbiol.* **13**, 777–786 (2015).
2. Clokie, M. R. J., Millard, A. D., Letarov, A. V. & Heaphy, S. Phages in nature. *Bacteriophage* **1**, 31–45 (2011).
3. Bernheim, A. & Sorek, R. The pan-immune system of bacteria: antiviral defence as a community resource. *Nat. Rev. Microbiol.* **18**, 113–119 (2020).
4. Dy, R. L., Richter, C., Salmond, G. P. C. & Fineran, P. C. Remarkable mechanisms in microbes to resist phage infections. *Annu. Rev. Virol.* **1**, 307–331 (2014).
5. Hampton, H. G., Watson, B. N. J. & Fineran, P. C. The arms race between bacteria and their phage foes. *Nature* **577**, 327–336 (2020).
6. Makarova, K. S., Wolf, Y. I., Snir, S. & Koonin, E. V. Defense islands in bacterial and archaeal genomes and prediction of novel defense systems. *J. Bacteriol.* **193**, 6039–6056 (2011).
7. Doron, S. et al. Systematic discovery of antiphage defense systems in the microbial pangenome. *Science* **359**, eaar4120 (2018).
8. Millman, A. et al. Bacterial retrons function in anti-phage defense. *Cell* **183**, 1551–1561.e12 (2020).
9. Lowey, B. et al. CBASS immunity uses CARF-Related effectors to sense 3′–5′- and 2′–5′-linked cyclic oligonucleotide signals and protect bacteria from phage infection. *Cell* **182**, 38–49.e17 (2020).
10. Gao, L. et al. Diverse enzymatic activities mediate antiviral immunity in prokaryotes. *Science* **369**, 1077–1084 (2020).
11. Koopal, B. et al. Short prokaryotic Argonaute systems trigger cell death upon detection of invading DNA. *Cell* **185**, 1471–1486.e19 (2022).
12. Millman, A. et al. An expanded arsenal of immune systems that protect bacteria from phages. *Cell Host Microbe* **30**, 1556–1569.e5 (2022).
13. Vassallo, C. N., Doering, C. R., Littlehale, M. L., Teodoro, G. I. C. & Laub, M. T. A functional selection reveals previously undetected anti-phage defence systems in the *E. coli* pangenome. *Nat. Microbiol.* **7**, 1568–1579 (2022).
14. Bernheim, A. et al. Prokaryotic viperins produce diverse antiviral molecules. *Nature* **589**, 120–124 (2021).
15. Bobonis, J. et al. Bacterial retrons encode phage-defending tri-partite toxin–antitoxin systems. *Nature* **609**, 144–150 (2022).
16. Zhang, T. et al. Direct activation of a bacterial innate immune system by a viral capsid protein. *Nature* **612**, 132–140 (2022).
17. Morehouse, B. R. et al. STING cyclic dinucleotide sensing originated in bacteria. *Nature* **586**, 429–433 (2020).
18. Ofir, G. et al. Antiviral activity of bacterial TIR domains via immune signalling molecules. *Nature* **600**, 116–120 (2021).
19. Tal, N. et al. Cyclic CMP and cyclic UMP mediate bacterial immunity against phages. *Cell* **184**, 5728–5739.e16 (2021).
20. Hogrel, G. et al. Cyclic nucleotide-induced helical structure activates a TIR immune effector. *Nature* **608**, 808–812 (2022).
21. Morehouse, B. R. et al. Cryo-EM structure of an active bacterial TIR–STING filament complex. *Nature* **608**, 803–807 (2022).
22. Duncan-Lowey, B. et al. Cryo-EM structure of the RADAR supramolecular anti-phage defense complex. *Cell* **186**, 987–998.e15 (2023).
23. Gao, Y. et al. Molecular basis of RADAR anti-phage supramolecular assemblies. *Cell* **186**, 999–1012.e20 (2023).
24. Shen, Z. et al. Oligomerization-mediated activation of a short prokaryotic Argonaute. *Nature* **621**, 154–161 (2023).
25. Gao, X. et al. Nucleic-acid-triggered NADase activation of a short prokaryotic Argonaute. *Nature* **625**, 822–831 (2023).
26. Antine, S. P. et al. Structural basis of Gabija anti-phage defence and viral immune evasion. *Nature* **625**, 360–365 (2024).
27. Li, J. et al. Structures and activation mechanism of the Gabija anti-phage system. *Nature* **629**, 467–473 (2024).
28. Gao, L. A. et al. Prokaryotic innate immunity through pattern recognition of conserved viral proteins. *Science* **377**, eabm4096 (2022).
29. Rostøl, J. T. et al. The Card1 nuclease provides defence during type III CRISPR immunity. *Nature* **590**, 624–629 (2021).
30. Yang, X.-Y., Shen, Z., Wang, C., Nakanishi, K. & Fu, T.-M. DdmDE eliminates plasmid invasion by DNA-guided DNA targeting. *Cell* **187**, 5253–5266.e16 (2024).
31. Loeff, L. et al. Molecular mechanism of plasmid elimination by the DdmDE defense system. *Science* **385**, 188–194 (2024).
32. Cheng, R. et al. A nucleotide-sensing endonuclease from the Gabija bacterial defense system. *Nucleic Acids Res.* **49**, 5216–5229 (2021).
33. Cheng, R. et al. Prokaryotic Gabija complex senses and executes nucleotide depletion and DNA cleavage for antiviral defense. *Cell Host Microbe* **31**, 1331–1344.e5 (2023).
34. Loeff, L., Walter, A., Rosalen, G. T. & Jinek, M. DNA end sensing and cleavage by the Shedu anti-phage defense system. *Cell* **188**, 721–733.e17 (2025).
35. Gu, Y. et al. Bacterial Shedu immune nucleases share a common enzymatic core regulated by diverse sensor domains. *Mol. Cell* **85**, 523–536.e6 (2025).
36. Bravo, J. P. K., Ramos, D. A., Fregoso Ocampo, R., Ingram, C. & Taylor, D. W. Plasmid targeting and destruction by the DdmDE bacterial defence system. *Nature* **630**, 961–967 (2024).
37. Sasaki, T. et al. Phage single-stranded DNA-binding protein or host DNA damage triggers the activation of the AbpAB phage defense system. *mSphere* **8**, e00372-23 (2023).
38. Tuck, O. T. et al. Genome integrity sensing by the broad-spectrum Hachiman antiphage defense complex. *Cell* **187**, 6914–6928.e20 (2024).
39. Shen, Z., Lin, Q., Yang, X.-Y., Fosuah, E. & Fu, T.-M. Assembly-mediated activation of the SIR2-HerA supramolecular complex for anti-phage defense. *Mol. Cell* **83**, 4586–4599.e5 (2023).
40. Tang, D. et al. Multiple enzymatic activities of a Sir2-HerA system cooperate for anti-phage defense. *Mol. Cell* **83**, 4600–4613.e6 (2023).
41. Ofir, G. et al. DISARM is a widespread bacterial defence system with broad anti-phage activities. *Nat. Microbiol.* **3**, 90–98 (2017).
42. Bravo, J. P. K., Aparicio-Maldonado, C., Nobrega, F. L., Brouns, S. J. J. & Taylor, D. W. Structural basis for broad anti-phage immunity by DISARM. *Nat. Commun.* **13**, 2987 (2022).
43. Hu, H. et al. Structure and mechanism of the Zorya anti-phage defense system. *Nature* https://doi.org/10.1038/s41586-024-08493-8 (2024).
44. Huiting, E. & Bondy-Denomy, J. A single bacterial enzyme i(NHI)bits phage DNA replication. *Cell Host Microbe* **30**, 417–419 (2022).
45. Bari, S. M. N. et al. A unique mode of nucleic acid immunity performed by a multifunctional bacterial enzyme. *Cell Host Microbe* **30**, 570–582.e7 (2022).
46. Sather, L. M. et al. A broadly distributed predicted helicase/nuclease confers phage resistance via abortive infection. *Cell Host Microbe* **31**, 343–355.e5 (2023).
47. Brouns, S. J. J. et al. Small CRISPR RNAs guide antiviral defense in prokaryotes. *Science* **321**, 960–964 (2008).
48. Jackson, R. N., Lavin, M., Carter, J. & Wiedenheft, B. Fitting CRISPR-associated Cas3 into the helicase family tree. *Curr. Opin. Struct. Biol.* **24**, 106–114 (2014).
49. Payne, L. J. et al. Identification and classification of antiviral defence systems in bacteria and archaea with PADLOC reveals new system types. *Nucleic Acids Res.* **49**, 10868–10878 (2021).
50. Yasui, R., Washizaki, A., Furihata, Y., Yonesaki, T. & Otsuka, Y. AbpA and AbpB provide anti-phage activity in *Escherichia coli*. *Genes Genet. Syst.* **89**, 51–60 (2014).
51. Lopatina, A., Tal, N. & Sorek, R. Abortive infection: bacterial suicide as an antiviral immune strategy. *Annu. Rev. Virol.* **7**, 371–384 (2020).
52. Steczkiewicz, K., Muszewska, A., Knizewski, L., Rychlewski, L. & Ginalski, K. Sequence, structure and functional diversity of PD-(D/E)

XK phosphodiesterase superfamily. *Nucleic Acids Res.* **40**, 7016–7045 (2012).

53. Watanabe, N., Takasaki, Y., Sato, C., Ando, S. & Tanaka, I. Structures of restriction endonuclease HindIII in complex with its cognate DNA and divalent cations. *Acta Cryst. D* **65**, 1326–1333 (2009).

54. Blatch, G. L. & Lässle, M. The tetratricopeptide repeat: a structural motif mediating protein-protein interactions. *Bioessays* **21**, 932–939 (1999).

55. Fairman-Williams, M. E., Guenther, U.-P. & Jankowsky, E. SF1 and SF2 helicases: family matters. *Curr. Opin. Struct. Biol.* **20**, 313–324 (2010).

56. Wu, B. et al. Structural basis for dsRNA recognition, filament formation, and antiviral signal activation by MDA5. *Cell* **152**, 276–289 (2013).

57. Wang, W. & Pyle, A. M. The RIG-I receptor adopts two different conformations for distinguishing host from viral RNA ligands. *Mol. Cell* **82**, 4131–4144.e6 (2022).

58. Kennedy, M. A. et al. Structures, activity and mechanism of the Type IIS restriction endonuclease PaqCI. *Nucleic Acids Res.* **51**, 4467–4487 (2023).

59. Teichmann, M., Dumay-Odelot, H. & Fribourg, S. Structural and functional aspects of winged-helix domains at the core of transcription initiation complexes. *Transcription* **3**, 2–7 (2012).

60. Arcus, V. OB-fold domains: a snapshot of the evolution of sequence, structure and function. *Curr. Opin. Struct. Biol.* **12**, 794–801 (2002).

61. Theobald, D. L., Mitton-Fry, R. M. & Wuttke, D. S. Nucleic acid recognition by OB-Fold proteins. *Annu. Rev. Biophys. Biomol. Struct.* **32**, 115–133 (2003).

62. Chen, W.-F. et al. Molecular mechanistic insights into drosophila DHX36-mediated g-quadruplex unfolding: a structure-based model. *Structure* **26**, 403–415.e4 (2018).

63. Song, X. et al. Catalytically inactive long prokaryotic Argonaute systems employ distinct effectors to confer immunity via abortive infection. *Nat. Commun.* **14**, 6970 (2023).

64. Wang, S. et al. Landscape of new nuclease-containing antiphage systems in *Escherichia coli* and the counterdefense roles of bacteriophage T4 genome modifications. *J. Virol.* **97**, e00599–23 (2023).

65. Tan, Y. Z. et al. Addressing preferred specimen orientation in single-particle cryo-EM through tilting. *Nat. Methods* **14**, 793–796 (2017).

66. Punjani, A., Rubinstein, J. L., Fleet, D. J. & Brubaker, M. A. cryoSPARC: algorithms for rapid unsupervised cryo-EM structure determination. *Nat. Methods* **14**, 290–296 (2017).

67. Zheng, S. Q. et al. MotionCor2: anisotropic correction of beam-induced motion for improved cryo-electron microscopy. *Nat. Methods* **14**, 331–332 (2017).

68. Chen, S. et al. High-resolution noise substitution to measure overfitting and validate resolution in 3D structure determination by single particle electron cryomicroscopy. *Ultramicroscopy* **135**, 24–35 (2013).

69. Kucukelbir, A., Sigworth, F. J. & Tagare, H. D. Quantifying the local resolution of cryo-EM density maps. *Nat. Methods* **11**, 63–65 (2014).

70. Jumper, J. et al. Highly accurate protein structure prediction with AlphaFold. *Nature* **596**, 583–589 (2021).

71. Brown, A. et al. Tools for macromolecular model building and refinement into electron cryo-microscopy reconstructions. *Acta Crystallogr. D Biol. Crystallogr.* **71**, 136–153 (2015).

72. Liebschner, D. et al. Macromolecular structure determination using X-rays, neutrons and electrons: recent developments in Phenix. *Acta Crystallogr. D Struct. Biol.* **75**, 861–877 (2019).

73. Williams, C. J. et al. MolProbity: more and better reference data for improved all-atom structure validation. *Protein Sci.* **27**, 293–315 (2018).

74. Barad, B. A. et al. EMRinger: side chain–directed model and map validation for 3D cryo-electron microscopy. *Nat. Methods* **12**, 943–946 (2015).

75. Hothorn, M. et al. Catalytic core of a membrane-associated eukaryotic polyphosphate polymerase. *Science* **324**, 513–516 (2009).

76. Katoh, K. & Standley, D. M. MAFFT multiple sequence alignment software version 7: improvements in performance and usability. *Mol. Biol. Evol.* **30**, 772–780 (2013).

77. Capella-Gutiérrez, S., Silla-Martínez, J. M. & Gabaldón, T. trimAl: a tool for automated alignment trimming in large-scale phylogenetic analyses. *Bioinformatics* **25**, 1972–1973 (2009).

78. Nguyen, L.-T., Schmidt, H. A., von Haeseler, A. & Minh, B. Q. IQ-TREE: a fast and effective stochastic algorithm for estimating maximum-likelihood phylogenies. *Mol. Biol. Evol.* **32**, 268–274 (2015).

79. Letunic, I. & Bork, P. Interactive Tree Of Life (iTOL) v5: an online tool for phylogenetic tree display and annotation. *Nucleic Acids Res.* **49**, W293–W296 (2021).

80. Gabler, F. et al. Protein sequence analysis using the mpi bioinformatics toolkit. *Curr. Protoc. Bioinform.* **72**, e108 (2020).

81. Wang, J. et al. The conserved domain database in 2023. *Nucleic Acids Res.* **51**, D384–D388 (2023).

Author contributions

Z.G. and T.Z. conceived the project. Y.C., Z.D., Y.O., C.F., Y.W., X.C., S.Z., W.W., and K.Y. performed the experiments. Y.C. and Z.D. prepared the cryo-EM samples and collected cryo-EM data. Z.G. determined the structures. P.T. provided phage collections. All authors analyzed the data and contributed to manuscript preparation. Y.C., Z.D., Z.G., and T.Z. wrote the manuscript.

Competing interests

The authors declare no competing interests.

Additional information

Supplementary information The online version contains supplementary material available at https://doi.org/10.1038/s41467-025-57851-1.

Correspondence and requests for materials should be addressed to Zeyuan Guan or Tingting Zou.

Peer review information *Nature Communications* thanks the anonymous reviewer(s) for their contribution to the peer review of this work. A peer review file is available.

Reprints and permissions information is available at http://www.nature.com/reprints

Publisher's note Springer Nature remains neutral with regard to jurisdictional claims in published maps and institutional affiliations.